Draft version May 5, 2025
Typeset using LaTeX **twocolumn** style in AASTeX631

Magnetic field amplification during a turbulent collapse

Axel Brandenburg[1,2,3,4] and Evangelia Ntormousi[5]

[1]*Nordita, KTH Royal Institute of Technology and Stockholm University, Hannes Alfvéns väg 12, SE-10691 Stockholm, Sweden*
[2]*The Oskar Klein Centre, Department of Astronomy, Stockholm University, AlbaNova, SE-10691 Stockholm, Sweden*
[3]*McWilliams Center for Cosmology & Department of Physics, Carnegie Mellon University, Pittsburgh, PA 15213, USA*
[4]*School of Natural Sciences and Medicine, Ilia State University, 3-5 Cholokashvili Avenue, 0194 Tbilisi, Georgia*
[5]*Scuola Normale Superiore, Piazza dei Cavalieri 7, 56126 Pisa, Italy*

ABSTRACT

The question of whether a dynamo can be triggered by gravitational collapse is of great interest, especially for the early Universe. Here, we employ supercomoving coordinates to study the magnetic field amplification from decaying turbulence during gravitational collapse. We perform three-dimensional simulations and show that for large magnetic Reynolds numbers, there can be exponential growth of the comoving magnetic field with conformal time before the decay of turbulence impedes further amplification. The collapse dynamics only affects the nonlinear feedback from the Lorentz force, which diminishes more rapidly for shorter collapse times, allowing nearly kinematic continued growth. We confirm that helical turbulence is more efficient in driving dynamo action than nonhelical turbulence, but this difference decreases for larger collapse times. We also show that for nearly irrotational flows, dynamo amplification is still possible, but it is always associated with a growth of vorticity—even if it still remains very small. In nonmagnetic runs, the growth of vorticity is associated with viscosity and grows with the Mach number. In the presence of magnetic fields, vorticity emerges from the curl of the Lorentz force.

Keywords: Magnetic fields (994); Hydrodynamics (1963)

1. INTRODUCTION

The ubiquitousness of dynamo action in various astrophysical plasmas has been hypothesized since the 1950s, but faced skepticism due to various anti-dynamo theorems (Cowling 1933; Hide & Palmer 1982). For a long time, the community focused on large-scale dynamos in the Sun (Parker 1955; Steenbeck et al. 1966) and galaxies (Parker 1971; Vainshtein & Ruzmaikin 1971). With the advance of powerful computers, small-scale dynamos at the scale of turbulence have received significant attention, starting with the early simulations of Meneguzzi et al. (1981). Kazantsev (1968) provided the current theoretical understanding of small-scale dynamos; see also Kulsrud & Anderson (1992) for an independent and more detailed derivation. By now, it is clear that three-dimensional turbulence always leads to dynamo action when the plasma is sufficiently well conducting; see Brandenburg & Ntormousi (2023) for a recent review. This behavior implies that part of the kinetic energy in turbulence is almost always converted into magnetic energy.

Characterizing turbulent dynamos is difficult because of the unsteady nature of the flow. For steady flows, we can always formulate an eigenvalue problem, provided the magnetic field is still weak and unaffected by the feedback from the Lorentz force, which affects the flow amplitude. It is even possible to prove that there is no eigenfunction with a non-vanishing eigenvalue when the magnetic diffusivity is strictly zero (Moffatt & Proctor 1985). Unsteady flows present a significant complication because, in that situation, the kinematic growth or decay of the magnetic field is no longer exponential. The problem becomes approachable if the flow is statistically steady, i.e., the level of turbulence can remain constant in time. In such cases, it has been shown that the energy spectrum grows at all wavenumbers at the same rate (Subramanian & Brandenburg 2014). This behavior is suggestive of the existence of an eigenfunction of the type discussed by Kazantsev (1968).

Many flows in astrophysics and plasma physics are not even statistically steady. Dynamo research in these cases is still in its infancy. One such situation is gravitational collapse, where the dynamo

problem has been studied using various numerical and analytical approaches (e.g. Sur et al. 2010, 2012; Federrath et al. 2011b; Xu & Lazarian 2020). The common problem these works face is identifying dynamo action when other amplification mechanisms like tangling or compression are also active. In this context, Brandenburg & Ntormousi (2022) emphasized that the Jeans instability drives predominantly irrotational motions that are unlikely to account for any dynamo action seen in the simulation.

Kinetic helicity (a measure of the alignment between velocity and vorticity) is not necessary for dynamo action, but if present, it lowers the critical conductivity needed to overcome the effects of Joule dissipation (Gilbert et al. 1988). Otherwise, resistive losses prematurely convert magnetic energy into heat before it can reach sufficient strength.

A collapsing flow can produce vorticity through viscosity (especially in shocks), the baroclinic term, and magnetic fields. However, which of these processes is active during collapse is currently unknown. To isolate effects related to the collapse dynamics, Irshad P et al. (2025) employed the supercomoving coordinates of Shandarin (1980), where the conformal time t is related to the physical time $t_{\rm ph}$ through $dt = dt_{\rm ph}/a^2$, and $a(t_{\rm ph})$ is the scale factor; see also Martel & Shapiro (1998) for a detailed presentation of the supercomoving coordinates in magnetohydrodynamics.

Irshad P et al. (2025) found super-exponential growth of the magnetic field as a result of the increasing turnover rate and saturation field strengths in excess of the expectations from flux freezing. They applied a solenoidal forcing function with and without kinetic helicity. The present work aims to study decaying turbulence, allowing not only for cases without initial kinetic helicity but also cases with or without initial vorticity (also called acoustic turbulence).

2. OUR MODEL

2.1. *Supercomoving coordinates*

We employ supercomoving coordinates using the same definition of the scale factor as Irshad P et al. (2025), i.e.,

$$a(t) = (1 + s^2 t^2/4)^{-1}, \tag{1}$$

where t is the conformal time, s is a free-fall parameter, which is related to the free-fall time $t_{\rm ff} = \pi/2s$. The physical time $t_{\rm ph}$ is then given by

$$t_{\rm ph}(t) = \int_0^t a^2(t')\,{\rm d}t', \tag{2}$$

which is defined in the range $0 \le t_{\rm ph} \le t_{\rm ff}$.

The supercomoving coordinates stretch the finite time singularity at $t_{\rm ff}$ to infinity while also limiting the comoving magnetic field strength according to

$$B = a^2 B_{\rm ph}, \tag{3}$$

where $B_{\rm ph}$ is the physical magnetic field.

2.2. *Governing equations*

We solve the MHD equations with an isothermal equation of state, where the pressure p and density ρ are related to each other through $p = \rho c_{\rm s}^2$ with $c_{\rm s} = {\rm const}$ being the isothermal sound speed. We apply an initial velocity field $\boldsymbol{u}$, which leads to a turbulent evolution. We also apply an initial seed magnetic field $\boldsymbol{B}$. To ensure that $\boldsymbol{B}$ remains solenoidal, we solve for the magnetic vector potential $\boldsymbol{A}$ so that $\boldsymbol{B} = \boldsymbol{\nabla} \times \boldsymbol{A}$. The evolution equations for $\boldsymbol{A}$, $\boldsymbol{u}$, and ρ are given by

$$\frac{\partial \boldsymbol{A}}{\partial t} = \boldsymbol{u} \times \boldsymbol{B} + \eta \nabla^2 \boldsymbol{A}, \tag{4}$$

$$\frac{{\rm D}\boldsymbol{u}}{{\rm D}t} = -c_{\rm s}^2 \boldsymbol{\nabla} \ln \rho + \rho^{-1} \left[a(t)\, \boldsymbol{J} \times \boldsymbol{B} + \boldsymbol{\nabla} \cdot (2\nu\rho \mathsf{S}) \right], \tag{5}$$

$$\frac{{\rm D} \ln \rho}{{\rm D}t} = -\boldsymbol{\nabla} \cdot \boldsymbol{u}, \tag{6}$$

where $\boldsymbol{J} = \boldsymbol{\nabla} \times \boldsymbol{B}/\mu_0$ is the current density with μ_0 being the vacuum permeability, $\boldsymbol{J} \times \boldsymbol{B}$ is the Lorentz force, S the rate-of-strain tensor with the components $\mathsf{S}_{ij} = \frac{1}{2}(\partial_i u_j + \partial_j u_i) - \frac{1}{3}\delta_{ij} \boldsymbol{\nabla} \cdot \boldsymbol{u}$ and ν is the kinematic viscosity.

2.3. *Initial conditions and parameters*

We consider a cubic domain of size L^3 with periodic boundary conditions. The lowest wavenumber in the domain is then $k_1 \equiv 2\pi/L$. Owing to the use of periodic boundary conditions, the mass in the domain is conserved, so the mean density is conserved, which defines our reference density $\rho_0 \equiv \overline{\rho}$. In the numerical simulations, we set $c_{\rm s} = k_1 = \rho_0 = 1$.

We construct our initial velocity in Fourier space (indicated by a tilde) as $\tilde{\boldsymbol{u}}(\boldsymbol{k}) = \mathsf{M}(\boldsymbol{k}) \boldsymbol{S}(\boldsymbol{k})$. Here,

$$S_j(\boldsymbol{k}) = r(\boldsymbol{k}, j)\, \frac{k_0^{-3/2} (k/k_0)}{1 + (k/k_0)^{17/6}}, \tag{7}$$

where $r(\boldsymbol{k}, j)$ is a Gaussian-distributed random number with zero mean and a variance of unity for each value of $\boldsymbol{k}$ and each direction j, k_0 is the peak wavenumber of the initial condition, and M is a matrix that consists of a superposition of a vortical and an irrotational contributions (Brandenburg & Scannapieco 2025):

$$\mathsf{M}_{ij}(\boldsymbol{k}) = (1 - \zeta)(\delta_{ij} - \hat{k}_i \hat{k}_j + \sigma {\rm i} \hat{k}_k \epsilon_{ijk}) + \zeta \hat{k}_i \hat{k}_j, \tag{8}$$

where $0 \leq \zeta \leq 1$ quantifies the irrotational fraction and $0 \leq \sigma \leq 1$ the helicity fraction. The extreme cases $\zeta = 0$ and $\zeta = 1$ correspond to vortical and irrotational flows, respectively, while $\sigma = 0$ and $\sigma = 1$ correspond to nonhelical and helical fields, respectively. The shell-integrated kinetic energy spectrum, $E_{\rm K}(k)$, which is normalized such that $\int E_{\rm K}(k)\,{\rm d}k = \rho_0\langle \boldsymbol{u}^2/2\rangle$, is initially $\propto k^4$ for $k < k_0$ and $\propto k^{-5/3}$ for $k > k_0$. The magnetic energy spectrum $E_{\rm M}(k)$ is normalized such that $\int E_{\rm M}(k)\,{\rm d}k = \langle \boldsymbol{B}^2/2\mu_0\rangle$ and initially of the same shape as $E_{\rm K}(k)$. We also compute the vortical energy spectrum $E_{\rm V}(k)$, which is normalized such that $\int k^2 E_{\rm V}(k)\,{\rm d}k = \rho_0\langle \boldsymbol{\omega}^2/2\rangle$, where $\boldsymbol{\omega} = \boldsymbol{\nabla}\times\boldsymbol{u}$ is the vorticity.

It is often convenient to express our results not in code units, where $c_{\rm s} = k_1 = \rho_0 = 1$, but in units of u_0 and k_0. Here, $u_0 \equiv \langle \boldsymbol{u}^2\rangle^{1/2}$ is the initial rms velocity. We also define a nondimensional magnetic field as

$$\mathcal{B}_i \equiv B_i/(\mu_0\rho_0 u_0^2)^{1/2}, \tag{9}$$

where $i = x, y, z$ refers to the three components, and $i = {\rm rms}$ or $i = {\rm ini}$ refer to the rms values of the magnetic field at the actual or the initial time, respectively. We also define the Mach and magnetic Reynolds numbers based on the initial velocity, ${\rm Ma}_0 = u_0/c_{\rm s}$ and ${\rm Re}_{\rm M} = u_0/\eta k_0$, respectively. The Mach number at the actual time is denoted by Ma. As a nondimensional measure of s, we define $\mathcal{S} = s/u_0 k_0$. When $\mathcal{S} < 1$ ($\mathcal{S} > 1$), the collapse is slower (faster) than the turnover rate of the turbulence.

In the following, we vary the input parameters $\mathcal{S}$, ζ, k_0/k_1, Ma, ${\rm Re}_{\rm M}$, and $\mathcal{B}_{\rm ini}$. In all cases presented below, the magnetic Prandtl number is unity, i.e., $\nu/\eta = 1$.

In the following, we display the conformal time in units of the initial turnover time, $(u_0 k_0)^{-1}$, where u_0 is the initial rms velocity. As in Brandenburg & Ntormousi (2022), we monitor the vortical and irrotational contributions to the turbulence, $\omega_{\rm rms} = \langle \boldsymbol{\omega}^2\rangle^{1/2}$ and $(\boldsymbol{\nabla}\cdot\boldsymbol{u})_{\rm rms} = \langle(\boldsymbol{\nabla}\cdot\boldsymbol{u})^2\rangle^{1/2}$, in terms of the quantities that have the dimension of a wavenumber,

$$k_{\boldsymbol{\nabla}\cdot\boldsymbol{u}} = (\boldsymbol{\nabla}\cdot\boldsymbol{u})_{\rm rms}/u_{\rm rms}, \tag{10}$$

$$k_{\boldsymbol{\omega}} = \omega_{\rm rms}/u_{\rm rms}. \tag{11}$$

These two values are expected to scale with k_0, which is why we usually present the ratios $k_{\boldsymbol{\nabla}\cdot\boldsymbol{u}}/k_0$ and $k_{\boldsymbol{\omega}}/k_0$.

We use for all simulations the Pencil Code (Pencil Code Collaboration et al. 2021). The resolution is either 512^3 or 1024^3, as indicated in Table 1, where we summarize all runs discussed in this paper. While higher resolution leads to more accurate results, the lower resolution computations produce qualitatively similar results; compare, for example, Runs 19 and 32, which have the same parameters. Both runs have almost the same vorticity and magnetic field evolution, but the lower resolution run has a slightly deeper minimum of k_ω/k_0, which results in a larger value of $\Delta\ln(k_\omega/k_0)$.

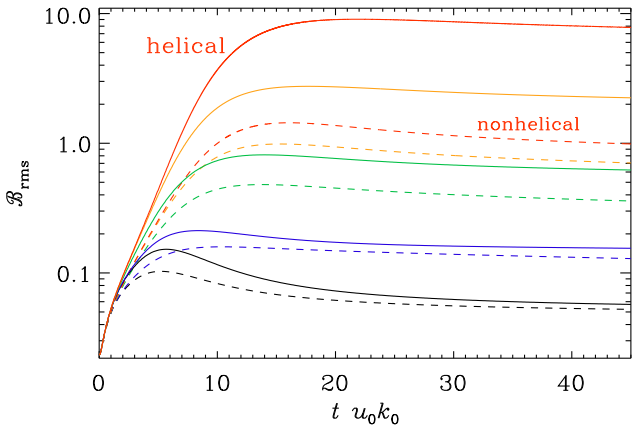

Figure 1. $\mathcal{S} = 0.1$ (black lines), 0.6 (blue lines), 2.8 (green lines), 11 (orange lines), and 56 (red lines). Solid (dashed) lines refer to cases with (without) initial kinetic helicity. For the nonhelical runs (dashed lines), the values of u_0 are slightly smaller, so $\mathcal{S}$ is correspondingly larger; see Table 1. Runs 3–7 and Runs 10–14.

3. RESULTS

3.1. *Growth vs physical and conformal time*

We have performed runs with different values of $\mathcal{S}$ using either helical ($\sigma = 1$) or nonhelical ($\sigma = 0$) turbulence, sometimes without irrotational contributions ($\zeta = 0$). Figure 1 shows that the larger the value of $\mathcal{S}$, the larger the final magnetic field strength. This is because the effective Lorentz force in Equation (5), $a\boldsymbol{J}\times\boldsymbol{B}$, diminishes more rapidly with time when $\mathcal{S}$ is larger, allowing the magnetic field to continue growing further. In supercomoving coordinates, the initial growth rate of the magnetic field is not affected by the value of $\mathcal{S}$. However, the growth rate is larger with than without kinetic helicity. On the other hand, at later times, when the magnetic field decays, the values are similar regardless of the presence of kinetic helicity.

In physical time, the magnetic field shows a steep increase just toward the end of the collapse; see Figure 2. Interestingly, the runs with large values of $\mathcal{S}$, which produce the strongest comoving magnetic fields, now yield the weakest physical fields when comparing the runs at the same fractional collapse time. This is because for the runs with large values of $\mathcal{S}$, the free-fall time is short, so the fractional times are larger, which effectively interchanges the order of the curves. This is demonstrated in the inset of Figure 2, where we show the same data, but now with time in units of the initial turnover time.

Table 1. Summary of the runs discussed in this paper. Here we list the nondimensional parameter $\mathcal{S}$; the physical values in code units are $s/c_s k_1 = 0.2$, 1, 5, 20, and 100. Column 7 gives $\mathrm{Re_M}$ (Re) for magnetic (nonmagnetic) runs. Dashes in columns 8–10 indicate the 8 nonmagnetic runs. For magnetic runs, dashes in columns 9 and 10 indicate decay. Run 39 corresponds to Run B of Brandenburg & Ntormousi (2022) and is discussed in Section 4.

Run	$\mathcal{S}$	σ	ζ	k_0/k_1	Ma_0	$\mathrm{Re_M}$ (Re)	$\mathcal{B}_{\rm ini}$	$\Delta \ln \mathcal{B}$	$\lambda/u_0 k_0$	$\Delta \ln(k_\omega/k_0)$	$(k_\omega/k_0)_{\rm max}$	resol.
1	0.1	1	0	10	0.18	1840	2.3×10^{-8}	8.33	0.52	0.39	7.09	512^3
2	0.1	1	0	10	0.18	1840	2.3×10^{-5}	6.62	0.52	0.39	7.09	512^3
3	0.1	1	0	10	0.18	1840	2.3×10^{-2}	1.88	1.00	0.31	6.46	512^3
4	0.6	1	0	10	0.18	1840	2.3×10^{-2}	2.21	1.03	0.22	5.93	512^3
5	2.8	1	0	10	0.18	1840	2.3×10^{-2}	3.56	1.03	0.30	6.43	512^3
6	11	1	0	10	0.18	1840	2.3×10^{-2}	4.77	1.03	0.36	6.82	512^3
7	56	1	0	10	0.18	1840	2.3×10^{-2}	5.96	1.03	0.39	7.04	512^3
8	0.2	0	0	10	0.13	1300	3.3×10^{-8}	4.27	0.37	0.33	6.97	512^3
9	0.2	0	0	10	0.13	1300	3.3×10^{-5}	4.22	0.37	0.33	6.97	512^3
10	0.2	0	0	10	0.13	1300	3.3×10^{-2}	1.49	0.97	0.14	5.70	512^3
11	0.8	0	0	10	0.13	1300	3.3×10^{-2}	1.92	0.97	0.17	5.91	512^3
12	3.8	0	0	10	0.13	1300	3.3×10^{-2}	3.03	0.98	0.29	6.66	512^3
13	15	0	0	10	0.13	1300	3.3×10^{-2}	3.75	0.98	0.33	6.92	512^3
14	77	0	0	10	0.13	1300	3.3×10^{-2}	4.12	0.98	0.33	6.97	512^3
15	0.2	0	0.10	10	0.12	1170	3.6×10^{-2}	1.41	0.34	0.11	5.50	512^3
16	0.2	0	0.50	10	0.08	800	5.4×10^{-2}	1.04	0.25	0.00	4.00	512^3
17	0.2	0	0.90	10	0.08	840	5.1×10^{-2}	0.31	0.04	0.25	0.94	512^3
18	0.2	0	0.95	10	0.09	880	4.9×10^{-2}	0.05	0.003	0.28	0.47	512^3
19	0.2	0	0.96	10	0.09	880	4.8×10^{-2}	0.02	0.001	0.26	0.38	512^3
20	0.2	0	0.97	10	0.09	890	4.8×10^{-2}	—	—	0.21	0.29	512^3
21	0.2	0	0.98	10	0.09	900	4.7×10^{-2}	—	—	0.13	0.20	512^3
22	0.2	0	0.99	10	0.09	910	4.7×10^{-2}	—	—	0.20	0.16	512^3
23	0.2	0	1	10	0.09	920	4.6×10^{-2}	—	—	0.30	0.14	512^3
24	0.1	0	1	20	0.09	920	—	—	—	0.01	0.07	1024^3
25	0.2	0	1	10	0.09	930	—	—	—	0.03	0.05	1024^3
26	0.4	0	1	5	0.09	940	—	—	—	0.38	0.04	1024^3
27	1.0	0	1	2	0.10	950	—	—	—	1.27	0.03	1024^3
28	0.5	0	0.95	10	0.04	220	—	—	—	0.09	0.23	512^3
29	0.1	0	0.95	10	0.18	890	—	—	—	0.31	0.71	1024^3
30	0.1	0	0.95	10	0.27	1330	—	—	—	0.43	1.00	1024^3
31	0.1	0	0.95	10	0.36	1780	—	—	—	0.51	1.31	1024^3
32	0.2	0	0.96	10	0.09	900	4.9×10^{-2}	0.02	0.001	0.17	0.38	1024^3
33	0.2	0	0.96	10	0.09	1800	4.9×10^{-2}	0.12	0.004	0.28	0.53	1024^3
34	0.2	0	0.96	10	0.09	4500	4.9×10^{-2}	0.51	0.008	0.53	0.79	1024^3
35	0.2	0	1	10	0.09	1870	9.4×10^{-3}	—	—	0.03	0.07	1024^3
36	0.2	0	1	10	0.09	1870	2.4×10^{-2}	—	—	0.17	0.09	1024^3
37	0.2	0	1	10	0.09	1870	4.7×10^{-2}	—	—	0.34	0.21	1024^3
38	0.2	0	1	10	0.09	1870	9.4×10^{-2}	—	—	0.25	0.48	1024^3
39	0.4	1	0	10	0.19	190	2.3×10^{-17}	8.32	0.42	0.01	4.29	2048^3

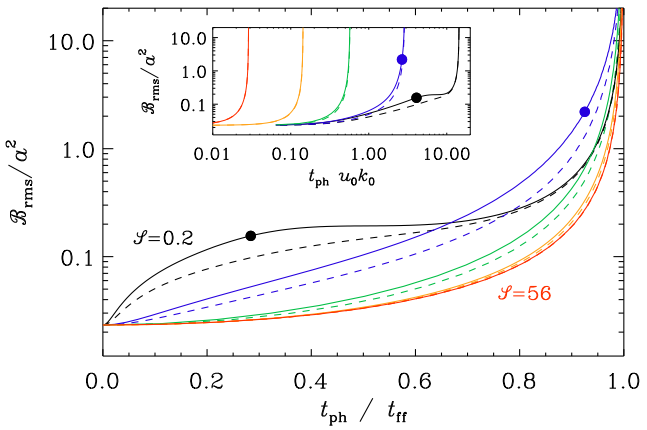

Figure 2. Same as Figure 1, but in physical units. Time is here normalized by the free-fall time. The black and blue dots on the black and blue curves denote the time until which the growth in Figure 1 was still approximately exponential. The inset shows the same, but now time is normalized by the initial turnover time. Runs 3–7 and Runs 10–14.

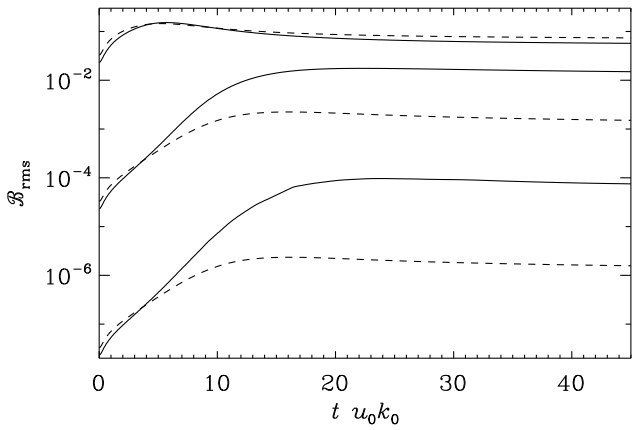

Figure 3. Same as Figure 1, but for 3 different initial field strengths. Runs 1–3 and Runs 8–10.

In Figure 2, we have also indicated the times where the initial exponential growth of the comoving magnetic field with conformal time terminates. For $\mathcal{S} = 0.1$ and 0.6, $\mathcal{B}_{\rm rms}/a^2$ has hardly increased by an order of magnitude. In particular, the growth of $\mathcal{B}_{\rm rms}/a^2$ versus physical time is not super-exponential, as claimed by Irshad P et al. (2025). Only for larger values of $\mathcal{S}$ is the growth super-exponential in physical coordinates, and exponential in comoving coordinates. For $\mathcal{S} \geq 2.8$, the times when exponential growth in comoving coordinates terminates are outside the plot range of Figure 2.

Given that the only effect of the collapse is on the Lorentz force, it is clear that the kinematic phase is completely independent of the collapse. This is shown quantitatively in Figure 3, where we see the magnetic field growth for different initial field strengths. For weak initial fields, the comoving magnetic field grows by more than three orders of magnitude. It could grow more strongly if the magnetic Reynolds number were larger. The growth is only limited by the competition between magnetic field amplification by the flow and the simultaneous decay of the flow. Similar results were already reported in Brandenburg et al. (2019), but without collapse dynamics ($a = 1$).

3.2. *Effect of the Lorentz force*

As we have seen from Figure 3, when the initial magnetic field strength is large, the early exponential growth diminishes more rapidly. This is the result of the effective Lorentz force in Equation (5) becoming comparable with the inertial term, which implies (Irshad P et al. 2025)

$$a^{1/2}B_{\rm rms} \lesssim u_{\rm rms}\sqrt{\mu_0\rho_0}. \tag{12}$$

This is demonstrated in Figure 4(a), where we compare the evolution of $a^{1/2}\mathcal{B}_{\rm rms}$ with that of $u_{\rm rms}/u_0$ for the same runs as those of Figures 1 and 2.

We see that Equation (12) is well obeyed for all runs. The largest values of $a^{1/2}\mathcal{B}_{\rm rms}$ are obtained for the runs with small values of $\mathcal{S}$. The effect of kinetic helicity is here surprisingly weak and the values of $a^{1/2}\mathcal{B}_{\rm rms}$ are only slightly smaller for the nonhelical runs than for the helical ones. For larger values of $\mathcal{S}$, on the other hand, the differences between helical and nonhelical runs are much larger and we see that the decay of $a^{1/2}$ is well overcompensated by the growth of $\mathcal{B}_{\rm rms}$ so that the product $a^{1/2}\mathcal{B}_{\rm rms}$ still shows a strong increase later in the evolution; see Figure 4(b), where we plot separately the evolutions of $a^{1/2}$ and $\mathcal{B}_{\rm rms}$.

We also see that for large values of $\mathcal{S}$ (short free-fall times), $a^{1/2}\mathcal{B}_{\rm rms}$ decays at early times and only shows growth after that. This is opposite to the case of small values of $\mathcal{S}$ and simply because at early times, $a^{1/2}$ decays faster than the exponential growth of $\mathcal{B}_{\rm rms}$. Only somewhat later, for $2 \lesssim tu_0k_0 \lesssim 10$, exponential growth prevails.

3.3. *Critical vorticity*

Numerical simulations have demonstrated in the past that vorticity is an important ingredient of dynamos (Haugen et al. 2004; Federrath et al. 2011a). Achikanath Chirakkara et al. (2021) did report dynamo action for purely irrotational driving, but this could perhaps still be explained by some residual vorticity in their simulations.

The apparent necessity of vorticity may be a limitation of current simulations, whose maximum magnetic

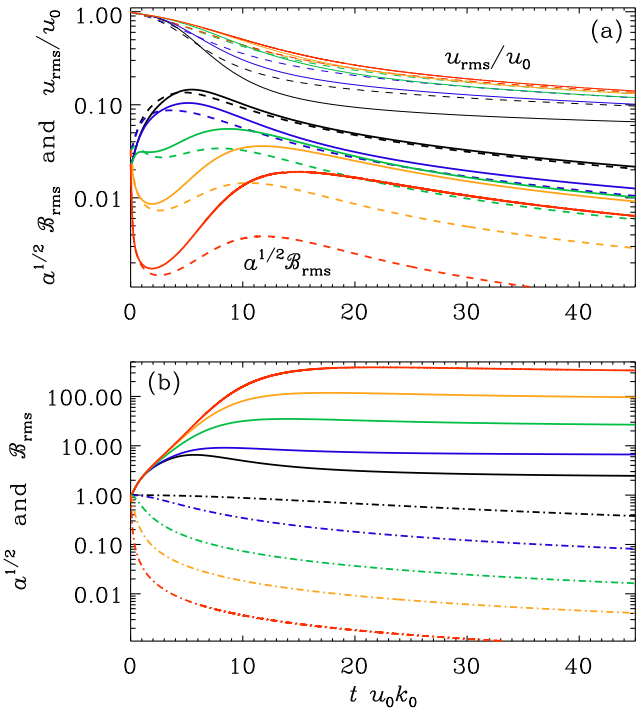

Figure 4. (a) Similar to Figure 1, but now $a^{1/2}\mathcal{B}_{\rm rms}$ (thicker lines) and the instantaneous rms velocity (thinner lines) are plotted. The order of the colors is the same as before, with black being for $\mathcal{S}=0.2$ and red for $\mathcal{S}=56$, and solid (dashed) lines refer to helical (nonhelical) initial flows. (b) Evolution separately for $a^{1/2}$ (dashed-dotted lines) and $\mathcal{B}_{\rm rms}$ (solid lines), again with the same colors as before with black being for $\mathcal{S}=0.2$ and red for $\mathcal{S}=56$. Runs 3–7 and Runs 10–14.

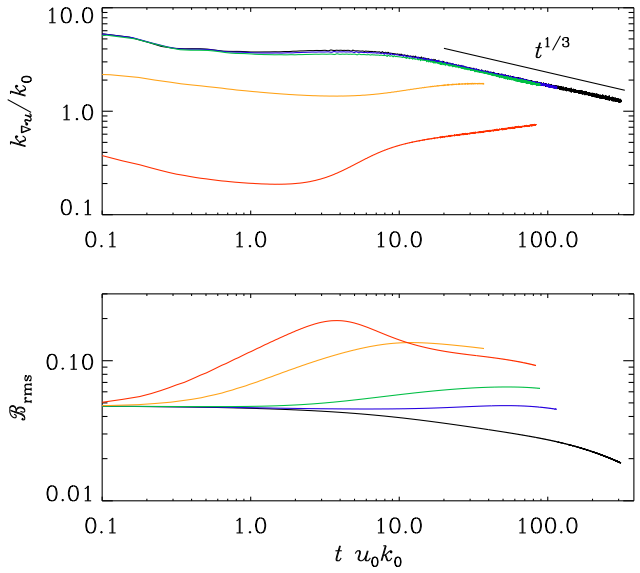

Figure 5. $k_{\nabla\cdot\boldsymbol{u}}/k_0$ (upper panel) and $\mathcal{B}_{\rm rms}$ (lower panel) for $\zeta=0.1$ (red), 0.5 (orange), 0.9 (green), 0.95 (blue), and 1 (black). Runs 15–18 and Run 23.

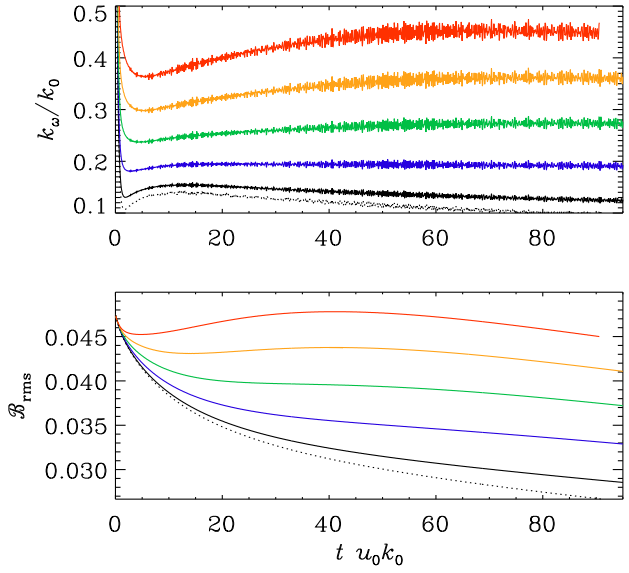

Figure 6. k_ω/k_0 (upper panel) and $\mathcal{B}_{\rm rms}$ (lower panel) for 1 (dotted black), 0.99 (solid black), 0.98 (blue), 0.97 (green), 0.96 (orange), and $\zeta=0.95$ (red). Runs 18–23.

Reynolds number may still not be large enough, because theoretically, small-scale dynamo action should also be possible for irrotational turbulence (Kazantsev et al. 1985; Martins Afonso et al. 2019). We can study this here in more detail by varying the value of ζ. In Figure 5 we plot the evolution of $k_{\boldsymbol{\nabla}\cdot\boldsymbol{u}}/k_0$ and $\mathcal{B}_{\rm rms}$ for runs with $\mathrm{Re_M}=900$ and several values of ζ. It is only when ζ is very close to unity that dynamo action ceases. This suggests that very small amounts of vorticity can suffice for successful dynamo action. The steady increase of $k_{\boldsymbol{\nabla}\cdot\boldsymbol{u}}/k_0$, which was also seen in the work of Brandenburg & Ntormousi (2022), is just a consequence of the more rapid decay of $(\boldsymbol{\nabla}\cdot\boldsymbol{u})_{\rm rms}$ compare to $u_{\rm rms}$.

In Figure 6 we focus on several more values close to unity and find that for $\mathrm{Re_M}=880$, the critical value of ζ is around 0.96. For larger values of ζ, there is no growth; see Runs 20–23 and Runs 35–38. However, the critical value of $1-\zeta$ decreases with increasing magnetic Reynolds number. For larger values of $\mathrm{Re_M}$, smaller amounts of vorticity suffice for dynamo action. This is shown in Figure 7, where we compare runs for $\zeta=0.96$ with different values of $\mathrm{Re_M}=900$, 1800, and 4500, using 1024^3 meshpoints. This value of ζ led to a vorticity that was the marginal value for obtaining growing magnetic fields for $\mathrm{Re_M}=900$. We see that, as we increase $\mathrm{Re_M}$, the episode of growth becomes longer and the maximum magnetic field larger.

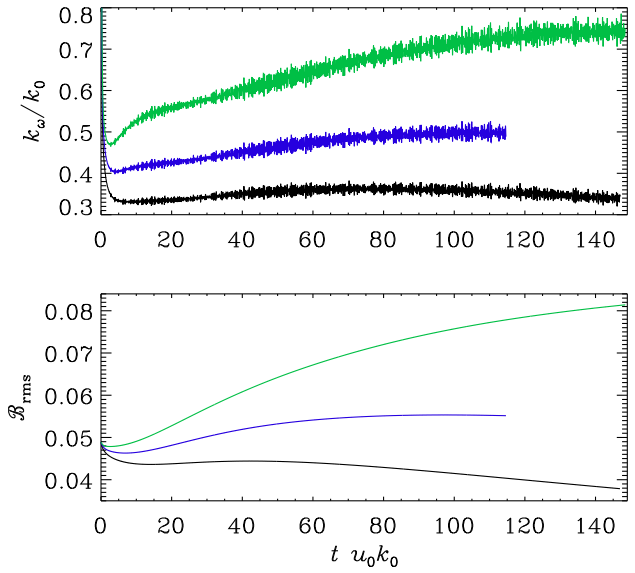

Figure 7. k_ω/k_0 (upper panel) and $\mathcal{B}_{\rm rms}$ (lower panel) for $\mathrm{Re_M} = 900$ (black), 1800 (blue), and 4400 (green). The frequency of the oscillations is $\omega \approx 15$. The resolution is in all cases 1024^3 mesh points. Runs 32–34.

It is of interest to define a Reynolds number based on the vorticity as (Haugen et al. 2004; Elias-López et al. 2023, 2024)

$$\mathrm{Re}_\omega = \omega_{\rm rms}/\nu k_0^2, \tag{13}$$

and to compute the critical value above which dynamo action occurs. Looking at Table 1, we see that the threshold of ζ between 0.96 and 0.97 corresponds to $k_\omega/k_0 = 0.38$ and 0.29, respectively, and with $\mathrm{Re_M} \approx 900$, the critical value is $\mathrm{Pr_M\,Re}_\omega = (k_\omega/k_0)\,\mathrm{Re_M} \approx 300$. This value is rather large, but it is unclear whether the dynamo onset is indeed determined predominantly by Re_ω. If dynamos do indeed work for purely acoustic turbulence ($\zeta = 1$), as found by Achikanath Chirakkara et al. (2021), the dynamo onset could not depend on Re_ω alone.

3.4. *Effect of scale separation*

We have seen from Figure 6 that for very small values of $1-\zeta$, the expected approach of k_ω to zero slows down in the sense that the values are almost the same for $\zeta = 1$ and $\zeta = 0.99$, and that for $\zeta = 0.98$ is further away. To check whether this is a consequence of finite scale separation, i.e., the ratio between the lowest wavenumber of the domain and the value of k_0 not being large enough, we present in Figure 8 runs with different values of k_0. As expected, we see that k_ω scales with k_0, so the ratio k_ω/k_0 varies only little and lies in the range $0.01 \le k_\omega/k_0 \le 0.02$ after about 10–30 turnover times. When we decrease the scale separation ratio to

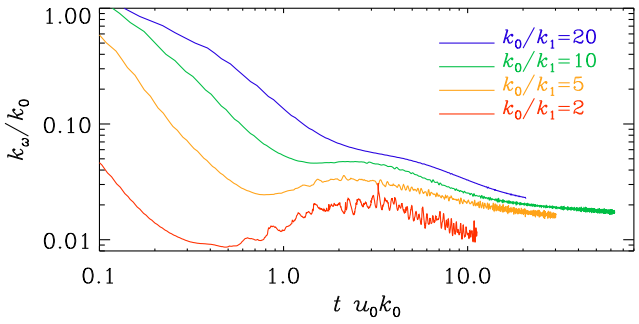

Figure 8. k_ω/k_0 for hydrodynamic runs with $\zeta = 1$, $\mathrm{Re_M} = 900$, and different values of k_0. For $k_0/k_1 = 10$, we also compare with the magnetic run with $\mathrm{Re_M} = 900$. Runs 24–27.

$k_0/k_1 = 2$, the run shows vigorous fluctuations. They may indicate that the numerical resolution becomes insufficient.

3.5. *Growth of vorticity*

In Figure 6, we have seen that for $\zeta = 0.95$, there can be growth of k_ω by a certain amount. It is possible that this is caused either by magnetic driving (Kahniashvili et al. 2012) or by what is known as magnetically assisted vorticity production (Brandenburg & Scannapieco 2025). It is therefore also useful to compare with the purely hydrodynamic case; see Table 1.

For an isothermal gas, there is no baroclinic term, which would be the main agent for producing vorticity in nonisothermal flows. There is also no rotation nor shear, both of which could lead to vorticity generation (Del Sordo & Brandenburg 2011; Elias-López et al. 2023, 2024). There remain only three possibilities for driving or amplifying vorticity: (i) through viscosity via gradients of the velocity divergence being inclined against density gradients, (ii) through magnetic driving or magnetically assisted vorticity production (Brandenburg & Scannapieco 2025), and (iii) through nonlinearity.

The growth of vorticity through nonlinearity may be motivated by the formal analogy with the induction equation when the magnetic field is replaced by the vorticity $\boldsymbol{\omega}$, i.e.,

$$\frac{\partial\boldsymbol{\omega}}{\partial t} = \boldsymbol{\nabla}\times(\boldsymbol{u}\times\boldsymbol{\omega}) + \dot{\boldsymbol{\omega}}_{\rm visc} + \dot{\boldsymbol{\omega}}_{\rm mag}, \tag{14}$$

where $\dot{\boldsymbol{\omega}}_{\rm visc} = \nu(\nabla^2\boldsymbol{\omega} + \boldsymbol{\nabla}\times\boldsymbol{G})$ is the curl of the viscous acceleration with $G_i = 2\mathsf{S}_{ij}\nabla_j \ln\rho$ being a vector characterizing the driving of vorticity even if it was vanishing initially (Mee & Brandenburg 2006; Brandenburg & Scannapieco 2025), and $\dot{\boldsymbol{\omega}}_{\rm mag} = \boldsymbol{\nabla}\times$

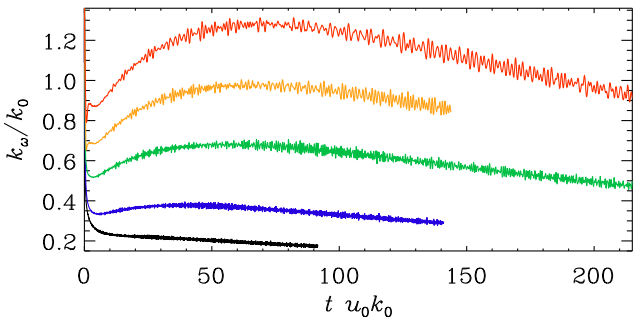

Figure 9. Evolution of k_ω/k_0 for different Mach numbers. Runs 28–31.

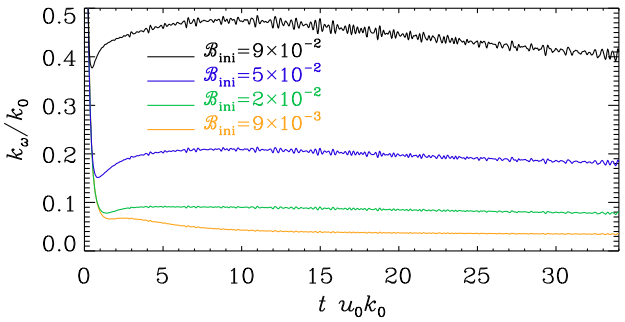

Figure 11. k_ω/k_0 for hydromagnetic runs with $\zeta = 1$, $\mathrm{Re_M} = 1900$, and different magnetic field strengths. Runs 35–38.

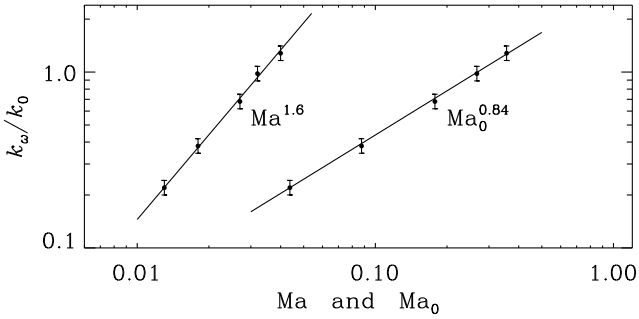

Figure 10. Scaling of k_ω/k_0 with the actual and initial Mach numbers, Ma and Ma_0, respectively. The slopes are 1.6 and 0.84, respectively. Runs 28–31.

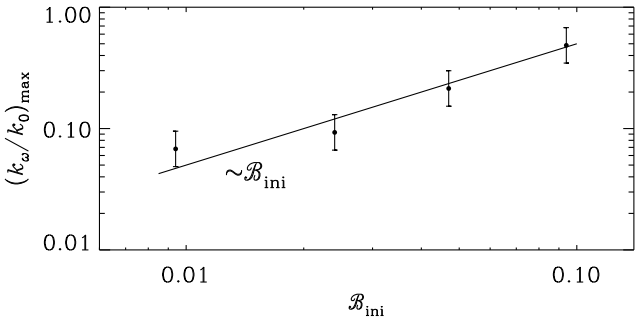

Figure 12. Dependence of the maximum of k_ω/k_0 on $\mathcal{B}_{\rm ini}$ for hydromagnetic runs with $\zeta = 1$, $\mathrm{Re_M} = 900$, and different magnetic field strengths. The straight line indicates a linear relationship. Runs 35–38.

$(\boldsymbol{J}\times\boldsymbol{B}/\rho)$ is the vorticity driving from the curl of the Lorentz force.

The analogy between induction and vorticity equations is obviously imperfect, because the velocity is here directly related to the vorticity. This analogy has been invoked by Batchelor (1950) to explain dynamo action, but here we rather use it to motivate the question whether vorticity can be amplified.

To distinguish between the various possibilities, we must vary the viscosity, the Mach number, and the initial magnetic field strength. One important clue is given by the fact that the occurrence of vorticity depends on the Mach number of the turbulence. This is demonstrated in Figure 9, where we plot the evolution of k_ω/k_0 for different Mach numbers. Figure 10 shows that k_ω scales with the actual and initial Mach numbers, Ma and Ma_0, respectively. The slopes for both scalings are different, and somewhat shallower than the nearly quadratic scaling found by Federrath et al. (2011a).

In all our runs, k_ω/k_0 reaches a maximum at some point. For runs 15–18, we see that $(k_\omega/k_0)_{\rm max}$ increases with increasing values of $\mathcal{B}_{\rm ini}$; see Figure 11. Figure 12 shows that this increase is linear and not quadratic, which means that the vorticity is magnetically driven rather than due to magnetically assisted growth; see Brandenburg & Scannapieco (2025) for details on this distinction. As seen from Table 1, the magnetic field decays for these runs, so there is no dynamo action.

3.6. *Spectral evolution*

In Figure 13, we show the evolution of $E_{\rm K}(k,t)$, $E_{\rm V}(k,t)$, and $E_{\rm M}(k,t)$ for Run 34. This is our run with the largest magnetic Reynolds number ($\mathrm{Re_M} = 4500$) and has only 4% vorticity ($\zeta = 0.96$), but shows clear dynamo action. Its time trace is shown in Figure 7.

We see that both $E_{\rm K}(k,t)$ and $E_{\rm V}(k,t)$ decay, while $E_{\rm M}(k,t)$ increases both at large and small wavenumbers. Overall, $E_{\rm V}(k)$ is almost a hundred times smaller than $E_{\rm K}(k,t)$, but, similarly to $E_{\rm M}(k,t)$, $E_{\rm V}(k)$ also shows a small temporal increase at small values of k. This is suggestive of magnetic vorticity production via an inverse cascade. Also, although $E_{\rm V}(k,t)$ decays in the inertial range, it bulges at $k/k_0 \approx 4$, which appears to be a direct consequence of magnetic driving.

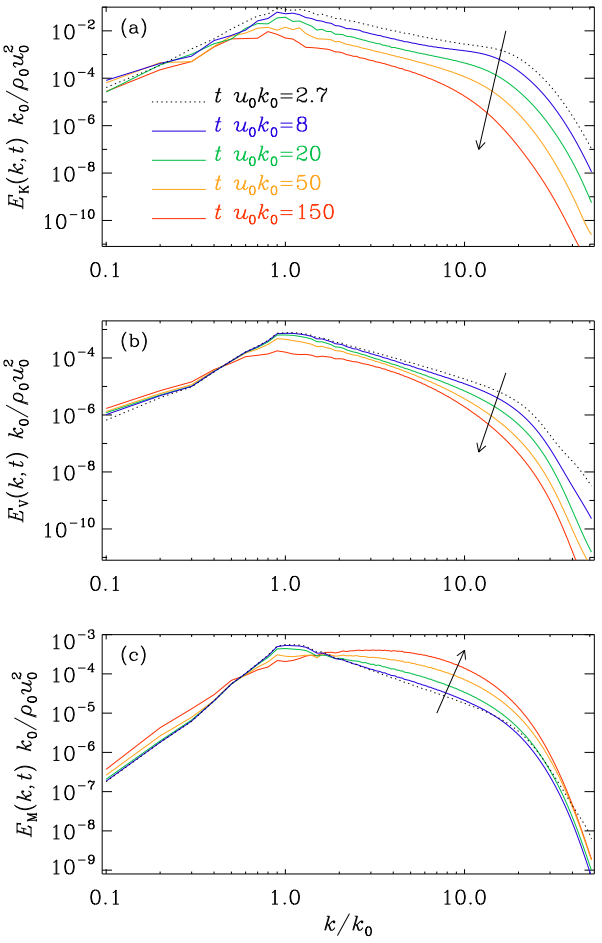

Figure 13. Evolution of $E_{\rm K}(k,t)$, $E_{\rm V}(k,t)$, and $E_{\rm M}(k,t)$ for Run 34. The arrows indicate the sense of time. The first time is shown as dotted lines to distinguish it better from the next one, for which $E_{\rm M}(k)$ is still very similar.

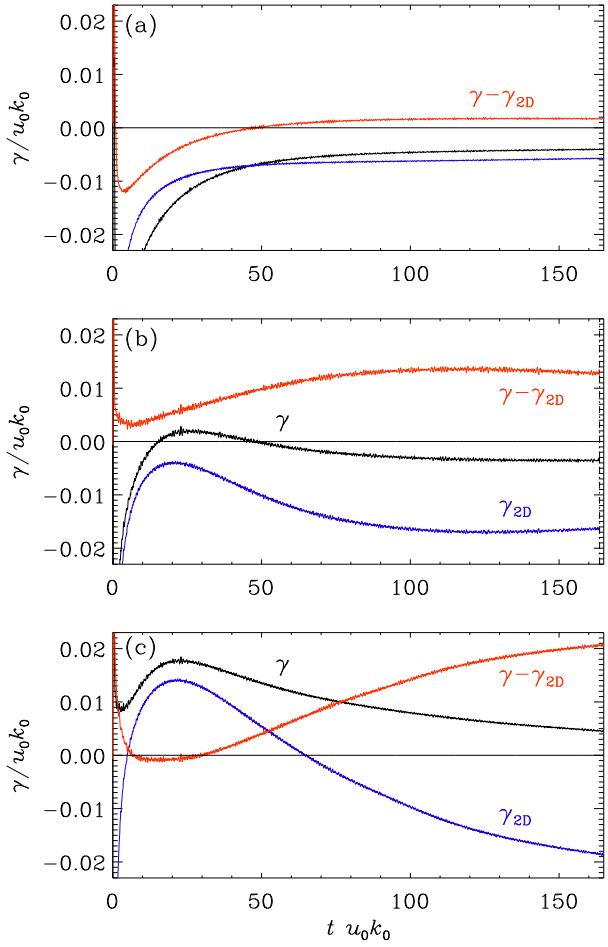

Figure 14. Evolution of the pseudo growth rate γ (black lines), with contributions from $\gamma_{\rm 2D}$ (blue lines) and the residual $\gamma-\gamma_{\rm 2D}$ (red lines), for Runs 23 (a), 32 (b), and 34 (c).

3.7. *Instantaneous growth rate*

For the magnetic energy to grow, the induction term $\boldsymbol{u}\times\boldsymbol{B}$ in Equation (4) has to overcome the dissipation term. In the evolution equation for the mean magnetic energy density, $\mathcal{E}_{\rm M}(t)\equiv\langle\boldsymbol{B}^2/2\mu_0\rangle$, the term

$$\langle\boldsymbol{J}\cdot(\boldsymbol{u}\times\boldsymbol{B})\rangle\equiv-W_{\rm L} \tag{15}$$

has to exceed the Joule dissipation, $Q_{\rm M}=\langle\mu_0\eta\boldsymbol{J}^2\rangle$. The instantaneous growth rate of magnetic energy can then be written as $\gamma=(-W_{\rm L}-Q_{\rm M})/\mathcal{E}_{\rm M}$. The first term, which can also be written as $W_{\rm L}=\langle\boldsymbol{u}\cdot(\boldsymbol{J}\times\boldsymbol{B})\rangle$, is the work done by the Lorentz force. When it is negative, kinetic energy is used to drive magnetic energy; see Equation (15).

Brandenburg & Ntormousi (2022) made use of the fact that in two dimensions (2D), when no action is possible, Equation (4) can be written as an advection–diffusion equation, i.e., $\mathrm{D}A/\mathrm{D}t=\eta\nabla^2A$, where A is the component of $\boldsymbol{A}$ that is normal to the 2D plane. This motivated them to decompose $W_{\rm L}$ by expanding $\boldsymbol{B}=\boldsymbol{\nabla}\times\boldsymbol{A}$ to get

$$-\langle\boldsymbol{J}\cdot(\boldsymbol{u}\times\boldsymbol{B})\rangle=\langle J_iu_j(A_{i,j}-A_{j,i}\rangle\equiv W_{\rm L}^{\rm 2D}+W_{\rm L}^{\rm 3D}. \tag{16}$$

Here, the first term is related to the advection term. The second term, $W_{\rm L}^{\rm 3D}=-\langle J_iu_jA_{j,i}\rangle$, vanishes in 2D. Thus, they identified $W_{\rm L}^{\rm 3D}$ with a contribution that characterizes the 3D nature of the system and used it as a proxy for dynamo action when it is large enough. They thus defined

$$\gamma_{\rm 2D}=-(W_{\rm L}^{\rm 2D}+Q_{\rm M})/\mathcal{E}_{\rm M},\quad \gamma_{\rm 3D}=-W_{\rm L}^{\rm 3D}/\mathcal{E}_{\rm M}, \tag{17}$$

so that $\gamma_{\rm 2D}+\gamma_{\rm 3D}=\gamma$.

In Figure 14, we plot the time dependences of γ, $\gamma_{\rm 2D}$, and $\gamma_{\rm 3D}=\gamma-\gamma_{\rm 2D}$ for Runs 23 (no dynamo, because k_ω is too small), 32 (weak dynamo), and 34 (strong dynamo, $\mathrm{Re_M}$ is the largest). We see that $\gamma_{\rm 2D}$ is always

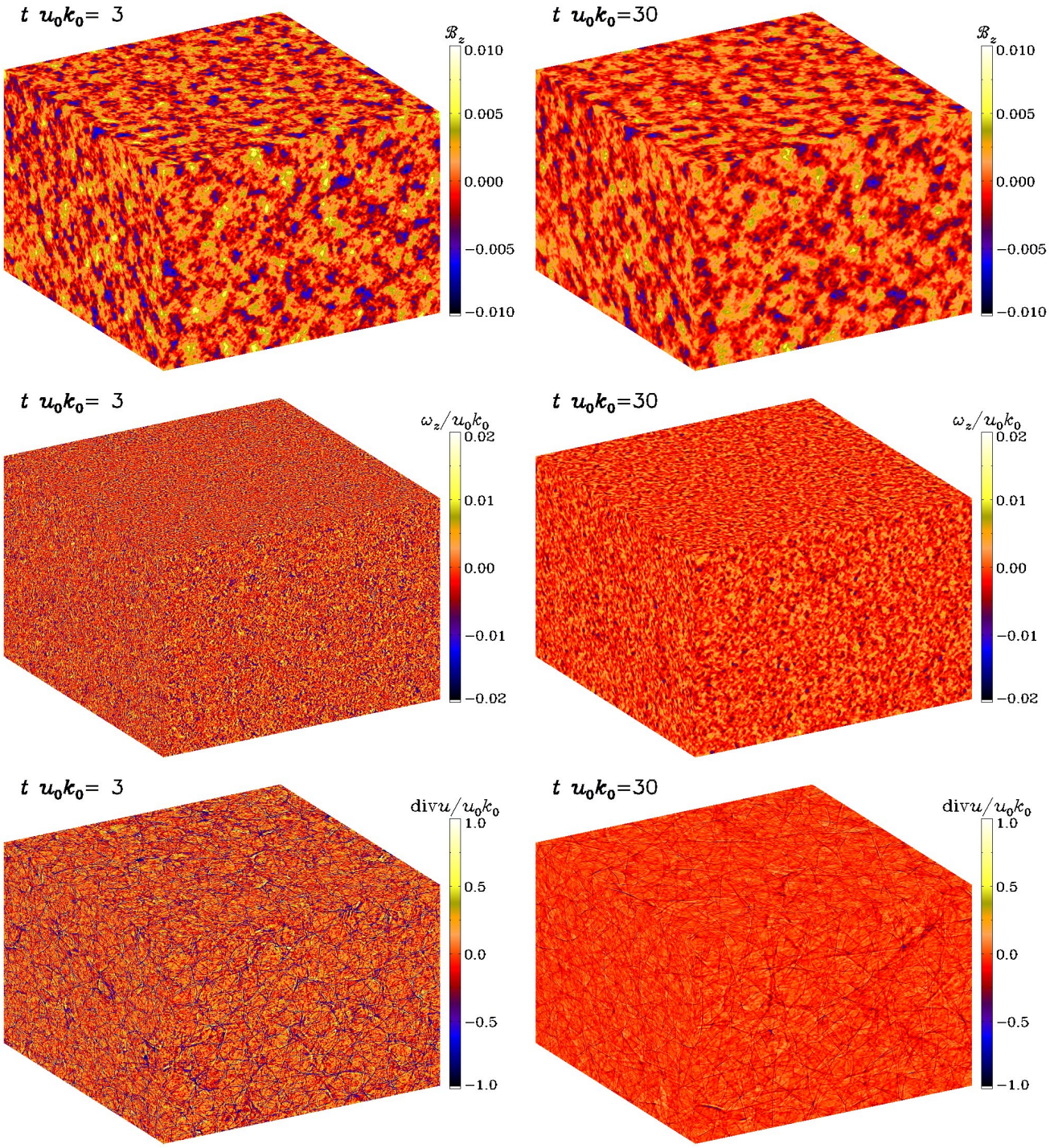

Figure 15. Visualizations of $\mathcal{B}_z$, ω_z/u_0k_0, and $\boldsymbol{\nabla}\cdot\boldsymbol{u}/u_0k_0$ for Run 37 at early and late times. Note that the domain is cubic, but the images have been stretched in the horizontal direction to take advantage of the full page size.

negative, except during an early phase for Run 34, which can be associated with strong 2D tangling of the initial magnetic field. When γ_{3D} is added to γ_{2D}, the resulting instantaneous growth rate is positive during the early part of the evolution of Run 32 and during the entire evolution of Run 34.

3.8. *Visualizations*

In Figure 15, we present visualizations of $\mathcal{B}_z$, ω_z/u_0k_0, and $\boldsymbol{\nabla}\cdot\boldsymbol{u}/u_0k_0$ for Run 37 at early and late times. There

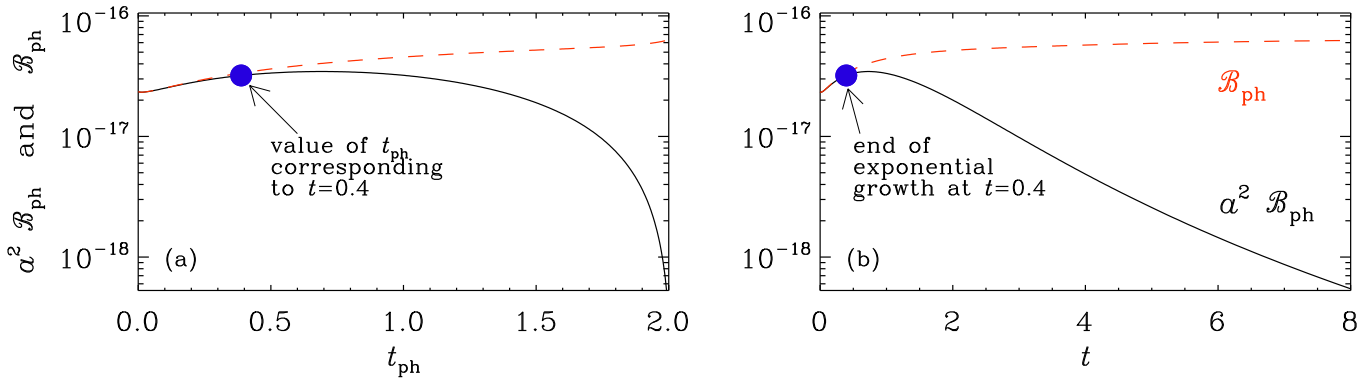

Figure 16. Physical magnetic field $\mathcal{B}_{\rm ph}$ (dashed red lines) and its comoving counterpart $a^2\mathcal{B}_{\rm ph}$ (black lines) versus physical time (a) and conformal time (b) for Run B from Brandenburg & Ntormousi (2022) and Run 39 of the present paper.

is no significance in us having chosen the z component of $\boldsymbol{B}$ and $\boldsymbol{\omega}$; all three components are statistically equivalent.

The magnetic field appears to preserve its initial length scale corresponding to $k = k_0$, and only the field strength becomes weaker with time. By contrast, the vorticity quickly develops small-scale patches that then grow to larger-scale patches at later times. Note also that the magnitude of ω_z/u_0k_0 (about 0.01) is comparable to that of $\mathcal{B}_z$. This is reminiscent of the findings of Kahniashvili et al. (2012), who reported a quantitative agreement between the spectra of vorticity and magnetic field.

For the velocity divergence, there is a much larger decrease from the time $tu_0k_0 = 3$ to $tu_0k_0 = 30$. As stated above, the compressive part of the velocity field, which is reflected in the values and the appearance of $\boldsymbol{\nabla}\cdot\boldsymbol{u}$, decreases more strongly with time than the vortical part, as reflected through the vorticity. We also see that, although the initial scales are rather small, they still seem to be sufficiently well resolved.

4. COMPARISON WITH PREVIOUS WORK

In our earlier paper (Brandenburg & Ntormousi 2022), we simulated gravitational collapse using numerical simulations of decaying turbulence in a Jeans-unstable domain at a resolution of 2048^2 mesh points. We only found a weak increase of the magnetic field with time. Given the knowledge of the collapse time from the simulations, we can replace the pressure-less free-fall time by the actual collapse time and express the evolution of the rms magnetic field in comoving coordinates. This allows us to see whether the growth is close to exponential during any time interval.

The result is shown in Figure 16, where we computed the conformal time and scale factor numerically based on Equation (1). Here we used the empirical value of $t_{\rm ff} \approx 2.016/c_{\rm s}k_1$, which yields $s \approx 0.78\,c_{\rm s}k_0$, and thus, since $u_0/c_{\rm s} = 0.19$ and $k_0/k_1 = 10$, we have $\mathcal{S} \approx 0.4$; see Table 1, where it is called Run 39. The physical values of the magnetic field are denoted by $\mathcal{B}_{\rm ph}$. We also plot the comoving values $a^2\mathcal{B}_{\rm ph}$ both versus physical and conformal time. Although there is a steady increase of $\mathcal{B}_{\rm rms}$, Figure 16(b) shows that the comoving magnetic field does not follow an exponential growth in conformal time, except for a very early time in the during $0 < tu_0k_0 \lesssim 0.4$.

To understand why the exponential phase is so short in this run, we compare its parameters with those of the other runs presented in this paper; see Table 1. The closest match is with Run 1. We see immediately that the main problem with Run 39 is the small value of the magnetic Reynolds number, which is 10 times smaller than that of Run 1. In spite of the high resolution of Run 39, the value of $\mathrm{Re_M}$ could not have been chosen larger because of the strong compression and large gradients suffered by the collapsing regions toward the end of the run. This highlights the main advantage of choosing supercomoving coordinates for collapse simulations.

5. CONCLUSIONS

When describing gravitational collapse in supercomoving coordinates, the governing equations of magnetohydrodynamics are similar to the original ones, except that now the scale factor appears in front of the Lorentz force. This reduces the effective Lorentz force, because $a(t)$ becomes progressively smaller with time. Therefore, in the limit of very short collapse times or large values of s, the evolution approaches essentially the kinematic evolution. This, however, does not mean unlimited continual growth, because the rms value of the turbulent intensity is declining.

As shown previously (Brandenburg et al. 2019), decaying turbulence leads to an episode of exponential growth if the magnetic Reynolds number is large enough. The larger it is, the longer is the episode of exponential

growth. This is essentially the result of a competition against the decay of turbulence, which lowers the instantaneous value of the magnetic Reynolds number as time goes on. The gravitational collapse changes this picture only little if we view the decay in supercomoving coordinates, because the collapse only affects the nonlinear dynamics, and this nonlinearity gets weaker with time.

In the work of Irshad P et al. (2025), forced turbulence was considered. Therefore, the magnetic field could always be sustained, but the source of such driving remains unclear. The superexponential growth that they reported, however, it still recovered in our decay simulations, unless the free-fall time is longer than the turnover time of the turbulence. In that case, the growth is actually subexponential.

Our present work has also shown that even very small amounts of vorticity can be sufficient to facilitate dynamo action. In particular, we find that the vorticity can grow in concert with the magnetic field.

Earlier work on turbulent collapse and dynamo action has suggested that gravitational collapse drives turbulence and enhanced it (Sur et al. 2012; Xu & Lazarian 2020; Hennebelle 2021). Our work casts doubt on this interpretation, because of two aspects. First, the collapse dynamics reduces the effective nonlinearity, resulting in stronger apparent field amplification by the turbulence, and second, there can be generation of vorticity both from viscosity and from the magnetic field itself. It should therefore be checked, whether these factors could have contributed to the earlier findings of collapse-driven turbulence.

As explained in Section 4, the transformation to supercomoving coordinates may also help analyzing existing simulations in physical coordinates. We argue that for homogeneous collapse simulations that do not utilize supercomoving coordinates, it is still useful to express such results in terms of comoving quantities and conformal time, because they might display exponential magnetic field growth that would be the perhaps strongest indication of dynamo action so far.

Our work has applications not just to interstellar clouds and primordial star formation (e.g., Schleicher et al. 2009; Hirano & Machida 2022; Sharda et al. 2020), but also to larger cosmological scales. Our results show that small amounts of vorticity might suffice to produce dynamo action even in decaying turbulence. This consideration is important for understanding magnetism in protohalos before the first stars form and their feedback drives sufficient turbulence for dynamo action (e.g., Schleicher et al. 2010).

Finally, our findings indicate that earlier simulations, including our own high-resolution simulations at 2048^3 meshpoints, may still have had insufficient resolution to follow the collapse and should be revisited using more idealized settings that allow the usage of a comoving frame.

We thank Fabio Del Sordo for helpful discussions on vorticity generation. We also acknowledge inspiring discussions with the participants of the program on "Turbulence in Astrophysical Environments" at the Kavli Institute for Theoretical Physics in Santa Barbara. This research was supported in part by the Swedish Research Council (Vetenskapsrådet) under Grant No. 2019-04234, the National Science Foundation under Grants No. NSF PHY-2309135, AST-2307698, and NASA Awards 80NSSC22K0825 and 80NSSC22K1265. We acknowledge the allocation of computing resources provided by the Swedish National Allocations Committee at the Center for Parallel Computers at the Royal Institute of Technology in Stockholm.

Software and Data Availability. The source code used for the simulations of this study, the Pencil Code (Pencil Code Collaboration et al. 2021), is freely available on https://github.com/pencil-code. The simulation setups and corresponding input and reduced output data are freely available on http://norlx65.nordita.org/~brandenb/projects/ascale-collapse.

REFERENCES

Achikanath Chirakkara, R., Federrath, C., Trivedi, P., & Banerjee, R. 2021, PhRvL, 126, 091103
Batchelor, G. K. 1950, RSPSA, 201, 405
Brandenburg, A., Kahniashvili, T., Mandal, S., et al. 2019, PhRvF, 4, 024608
Brandenburg, A., & Ntormousi, E. 2022, MNRAS, 513, 2136
—. 2023, ARA&A, 61, 561
Brandenburg, A., & Scannapieco, E. 2025, ApJ, 983, 105
Cowling, T. G. 1933, MNRAS, 94, 39
Del Sordo, F., & Brandenburg, A. 2011, A&A, 528, A145
Elias-López, A., Del Sordo, F., & Viganò, D. 2023, A&A, 677, A46
—. 2024, A&A, 690, A77
Federrath, C., Chabrier, G., Schober, J., et al. 2011a, PhRvL, 107, 114504
Federrath, C., Sur, S., Schleicher, D. R. G., Banerjee, R., & Klessen, R. S. 2011b, ApJ, 731, 62

Gilbert, A. D., Frisch, U., & Pouquet, A. 1988, GApFD, 42, 151
Haugen, N. E. L., Brandenburg, A., & Mee, A. J. 2004, MNRAS, 353, 947
Hennebelle, P. 2021, A&A, 655, A3
Hide, R., & Palmer, T. N. 1982, GApFD, 19, 301
Hirano, S., & Machida, M. N. 2022, ApJL, 935, L16
Irshad P, M., Bhat, P., Subramanian, K., & Shukurov, A. 2025, arXiv e-prints, arXiv:2503.19131
Kahniashvili, T., Brandenburg, A., Campanelli, L., Ratra, B., & Tevzadze, A. G. 2012, PhRvD, 86, 103005
Kazantsev, A. P. 1968, JETP, 26, 1031
Kazantsev, A. P., Ruzmaikin, A. A., & Sokolov, D. D. 1985, ZhETF, 61, 285
Kulsrud, R. M., & Anderson, S. W. 1992, ApJ, 396, 606
Martel, H., & Shapiro, P. R. 1998, MNRAS, 297, 467
Martins Afonso, M., Mitra, D., & Vincenzi, D. 2019, RSPSA, 475, 20180591
Mee, A. J., & Brandenburg, A. 2006, MNRAS, 370, 415
Meneguzzi, M., Frisch, U., & Pouquet, A. 1981, PhRvL, 47, 1060
Moffatt, H. K., & Proctor, M. R. E. 1985, JFM, 154, 493
Parker, E. N. 1955, ApJ, 122, 293
—. 1971, ApJ, 163, 255
Pencil Code Collaboration, Brandenburg, A., Johansen, A., et al. 2021, JOSS, 6, 2807
Schleicher, D. R. G., Banerjee, R., Sur, S., et al. 2010, A&A, 522, A115
Schleicher, D. R. G., Galli, D., Glover, S. C. O., et al. 2009, ApJ, 703, 1096
Shandarin, S. F. 1980, Astrophysics, 16, 439
Sharda, P., Federrath, C., & Krumholz, M. R. 2020, MNRAS, 497, 336
Steenbeck, M., Krause, F., & Rädler, K. H. 1966, Zeitschrift Naturforschung Teil A, 21, 369
Subramanian, K., & Brandenburg, A. 2014, MNRAS, 445, 2930
Sur, S., Federrath, C., Schleicher, D. R. G., Banerjee, R., & Klessen, R. S. 2012, MNRAS, 423, 3148
Sur, S., Schleicher, D. R. G., Banerjee, R., Federrath, C., & Klessen, R. S. 2010, ApJL, 721, L134
Vainshtein, S. I., & Ruzmaikin, A. A. 1971, AZh, 48, 902
Xu, S., & Lazarian, A. 2020, ApJ, 899, 115